Gas-Phase $Ni^+(^2D_{5/2}) + n\text{-}C_4H_{10}$ Reaction Dynamics in Real Time: Experiment and Statistical Modeling Based on Density Functional Theory

Margareta Blomberg*

Department of Physics, University of Stockholm, Box 6730, S-113 85 Stockholm, Sweden

Sung Soo Yi, Robert J. Noll, and James C. Weisshaar*

Department of Chemistry, 1101 University Avenue, University of Wisconsin-Madison, Madison, WI 53706-1396

Received: May 12, 1999; In Final Form: July 1, 1999

A beam of $Ni^+(^2D_{5/2})$ is formed at a sharp zero of time by resonant two-photon ionization with a nanosecond dye laser pulse and crossed with a beam of *n*-butane-h_{10} or *n*-butane-d_{10} gas. The ion−molecule reaction occurs under single-collision conditions in field-free space in the extraction region of a time-of-flight mass spectrometer. After a variable time delay $t_{ext} = 0.5-8\ \mu$s, a fast high-voltage pulse extracts product ions and residual reactant ions into a field-free flight tube for mass analysis. Analysis of the metastable decay of $NiC_4H_{10}^+$ complexes from tailing of fragment ion peaks and from retarding field separation reveals detailed information about the formation of elimination products (primarily ethane and H_2) and the decay back to Ni^+ reactants in different time windows from 0.2 to 25 μs after initiation of the collision. To understand the data, we have used density functional theory in its B3LYP variant to locate and characterize the geometries, potential energies, and vibrational frequencies of some 25 stationary points on the ground-state doublet potential energy surface for $Ni^+ + n\text{-}C_4H_{10}$. As in earlier work on $Ni^+ + C_3H_8$, we find that the highest potential energy points along pathways leading to H_2, CH_4, and C_2H_6 elimination are multi-center transition states (MCTSs) involving simultaneous motion of many atoms about the Ni^+ center. The extensive body of information from the electronic structure calculations provides realistic input to a statistical (RRKM) rate model of the reaction. Many details of the time evolution of long-lived complexes for both $NiC_4H_{10}^+$ and $NiC_4D_{10}^+$ can be understood semiquantitatively when conservation of angular momentum is accounted for in approximate fashion. In our best model, the energetics of the MCTSs leading to C_2H_6 and H_2 elimination must be adjusted downward by 2−3 and 7 kcal/mol, respectively, from the calculated barrier heights. According to this model, essentially all of the C_2H_6 and H_2 products come from initial insertion of Ni^+ into the central CC bond, the weakest bond in the alkane. The lowest energy path to H_2 elimination is novel, involving initial insertion into the central CC bond followed by simultaneous migration of *two* β-hydrogens toward each other while being stabilized by the metal cation center. Insertion into a terminal CC bond or into either type of CH bond leads to substantially higher energy MCTSs that are likely unimportant at low collision energy.

I. Introduction

The rapid development of density functional theory (DFT)[1] continues to open new areas of chemistry to detailed investigation by electronic structure theory. In solution-phase organometallic chemistry, DFT is already providing new insights into reaction mechanisms. For systems involving transition-metal species, it is important to calibrate the quantitative accuracy of different theoretical methods. For this purpose, reactions of gas-phase transition-metal atoms (M and M^+)[2−4] provide a relevant degree of electronic complexity (due to the presence of open d-subshells and many low-lying electronic states) without the additional computational burden of ligands and solvent present in condensed-phase chemistry. Comparisons between experimental and calculated gas-phase bond dissociation energies[5] provide one test of theory. Equally important are detailed measurements that provide information about the energetics of key transition states in organometallic reactions. Since subtle differences in transition-state energies typically control reaction efficiency and product branching, the ability to predict even transition-state energies on a relative scale with accuracy of a few kcal/mol would provide a powerful tool for the design of catalysts.

In an earlier pair of papers,[6,7] we obtained time-resolved experimental information about the decay of bimolecular collision complexes for the reaction $Ni^+ + C_3H_8$. We also applied DFT to the ground-state $NiC_3H_8^+$ potential energy surface and built a detailed statistical rate model of the reaction based on theory. The agreement between the model and a wide variety of experiments allowed us to gain new qualitative insights into the reaction mechanism. Here we extend this approach to the reaction of ground-state $Ni^+(^2D_{5/2})$ with $n\text{-}C_4H_{10}$ at collision energies of 0.01 eV (0.2 kcal/mol) and 0.21 eV (4.8 kcal/mol) under carefully controlled, single-collision, crossed-beam conditions. A preliminary report on part of the data has already appeared.[8,9] The state-specific Ni^+ beam is formed at a sharp zero of time by resonant two-photon ionization (R2PI) using a nanosecond dye laser. The subsequent formation of long-lived $NiC_4H_{10}^+$ complexes (1a) and their evolution back to Ni^+ reactants and forward to C_2H_6, CH_4, and H_2 elimination products (1b, 1c, 1d) is monitored in real time on a scale as short as 0.2 μs using pulsed time-of-flight mass spectrometry. Long-lived complexes that survive extraction may fragment

* Authors to whom correspondence should be addressed. E-mail addresses: mb@physto.SE; weisshaar@chem.wisc.edu.

10.1021/jp991561j CCC: $18.00
Published on Web 08/12/1999

$$Ni^+ + n\text{-}C_4H_{10} \rightarrow \begin{cases} NiC_4H_{10}^+ & (1a) \\ NiC_4H_{10}^+ + C_2H_6 & (1b) \\ NiC_3H_6^+ + CH_4 & (1c) \\ NiC_4H_8^+ + H_2 & (1d) \end{cases}$$

in the field-free flight tube; we can further analyze the dynamics by using retarding fields[10] to separate these fragments.

The result is a set of time-resolved branching fractions measured under carefully controlled reaction conditions. These provide a new benchmark for comparison with theoretical work. We present electronic structure calculations based on the B3LYP[1] variant of DFT of the energetics of potential wells and transition states for the same $Ni^+ + C_4H_{10}$ reaction. The lowest energy paths to the predominant C_2H_6 and H_2 products both involve initial insertion of Ni^+ into the central CC bond, the weakest bond in the *n*-butane molecule. Subsequent branching and rearrangement over two alternative multi-center transition states (MCTSs) leads to elimination products. Other pathways lie much higher in energy. The moments of inertia and vibrational frequencies from theory allow us to build a realistic, comprehensive rate model of the reaction. The dynamics are treated using statistical (RRKM)[11−13] rate theory on a single adiabatic potential energy surface. Much as in $Ni^+ + C_3H_8$,[7] we find that substantial downward adjustment by 3−7 kcal/mol of the energies from B3LYP theory brings the rate calculations into good agreement with experimental data, including elimination branching fractions and H/D isotope effects. The ability of B3LYP theory to discover new reaction pathways and to achieve semiquantitative agreement with experiment for such a complex reaction is highly encouraging.

II. Experimental Section

A. Crossed-Beam Measurements. The crossed-beam apparatus and its usual operating parameters have been described previously.[6,14,15] In the source chamber, gas-phase nickel atoms are produced in a laser ablation source and seeded into an argon beam, which is skimmed and collimated. Electric fields strip ions from the beam. In the interaction chamber, the nickel atoms are ionized by a pulsed dye laser, initiating bimolecular ion−molecule collisions. The Ni^+ cations react in field-free space with hydrocarbon molecules from a second pulsed valve. After a suitable reaction delay, a high-voltage pulse extracts reactant and product ions into the time-of-flight mass spectrometer (TOF/MS) for analysis.

The frequency-doubled dye laser (10 ns fwhm, 323.384 nm, <250 μJ/pulse) intersects the atomic beam and resonantly photoionizes Ni via the $z^3G_5^\circ \leftarrow a^3F_4$ transition at 30 923 cm^{-1}.[16] Absorption of two such photons creates Ni^+ exclusively in the $^2D_{5/2}$ state. The two-photon energy is only 227 cm^{-1} above the ionization potential of 61 619 cm^{-1}.[17] The nearest Ni^+ excited state is $^2D_{3/2}$ at 1507 cm^{-1} above the IP. A log−log plot of Ni^+ ion yield vs laser pulse energy is linear with slope of unity, consistent with a two-photon process whose first step is saturated.

The metal ion velocity is that of the neutral beam, $(5.8 \pm 0.5) \times 10^4$ cm/s. The packet of Ni^+ ions (1000−8000 ions/shot) intersects the beam of hydrocarbon molecules in the extraction region of a Wiley−McLaren[18] time-of-flight mass spectrometer. Neat *n*-butane gas ($-h_{10}$ from Matheson, >99.9% purity, $-d_{10}$ from Cambridge Isotopes, >98% D atoms) expands from a second 0.5 mm pulsed nozzle; the butane beam is pseudo-skimmed (i.e., not differentially pumped) by a set of home-built rectangular knife edges. The butane velocity is $(6.7 \pm 1.0) \times 10^4$ cm/s. The typical *n*-butane pressure behind the nozzle is 60 Torr. From Fenn and Gallagher,[19] we estimate that the *n*-butane is cooled to a vibrational temperature of about 50 K. There is no evidence of reactions with butane clusters. Plots of product yield vs hydrocarbon backing pressure are linear from 10 to 120 Torr, indicating that single-collision conditions are obtained at 60 Torr.

By changing the angle between the Ni^+ and *n*-butane beams, we can vary the collision energy in coarse steps. We have conducted the experiments at two collision energies, nominal 0.011 ± 0.010 eV (0.25 ± 0.23 kcal/mol) and 0.21 ± 0.09 eV (4.8 ± 2.1 kcal/mol). The estimated uncertainties reflect worst-case analyses; the larger collision energy is better defined. We believe the "nominal 0.01 eV" energy includes a distribution peaked at 0.01 eV and lying below 0.02 eV = 0.5 kcal/mol.

The 10 ns laser pulse initiates ion−molecule collisions at a sharply defined starting time. After a variable delay time that allows collisions to occur, reactant and product ions are extracted at time t_{ext} into the TOF-MS for analysis. We can obtain useful signals for extraction times in the range $0.2\ \mu s \le t_{ext} \le 8\ \mu s$. At t_{ext}, high-voltage pulses (1−1.5 kV) are applied to the ion extraction plates, sending reactant and product ions toward the detector. The mass resolution ($m/\Delta m$) is >250 for products near 100 amu. Ions are detected with a microchannel plate (Galileo FTD-2003) operated at 6×10^7 gain. Detector output is 50-Ω coupled to a LeCroy 9400 digital oscilloscope without further amplification. The detector dynamic range cannot simultaneously accommodate the Ni^+ signal and product ion signal. Therefore, a small set of electrodes mounted in the drift region is pulsed at the appropriate time to deflect Ni^+ ions away from the detector, acting as a mass gate.

Mass spectra are complicated by the presence of five Ni isotopes at 58 amu (68%), 60 amu (26%), 61 amu (1.3%), 62 amu (3.7%), and 64 amu (1.2%) plus the presence of one ^{13}C in some 4% of the *n*-butane molecules. Quantitative product branching ratios are based on the areas under well-resolved product peaks of the majority isotope ^{58}Ni. In cases of mass interferences, areas of blended peaks were scaled to the ^{58}Ni basis using published Ni isotope abundances.

It is important to distinguish clearly two different time scales that we will refer to frequently. The first, which we have already called t_{ext}, is the experimental time window during which the Ni^+ and C_4H_{10} reactant beams are "in contact" and collisions at a well-defined energy may occur. This is the time between the ionizing laser pulse and the ion extraction pulse. The second time, which we simply call *t*, refers to the time since a long-lived complex was formed in a bimolecular collision. It is the sort of time that appears naturally in the kinetics model for the unimolecular decay of a population of $Ni^+(C_4H_{10})$ complexes which were all present at $t = 0$. Because our experiment is firmly in the single-collision limit, we create collision complexes with a uniform distribution of initiation times over a time window of width t_{ext}. When we sample the fate of this collection of complexes at a particular real experimental time after the ionizing laser pulse, we sample complexes that have evolved over a corresponding distribution of times *t* after initiation. In comparing kinetics model results with experiment, we properly average over this distribution.

B. Analysis of Metastable Decay by Retarding Potential Method. Under our carefully controlled reaction conditions, the product mass spectra reveal long-lived $NiC_4H_{10}^+$ collision complexes (reaction 1a). These complexes have survived extraction intact, since they arrive at the detector at appropriate times for adduct ions. Under our single-collision conditions, the

complexes are metastable. They have sufficient energy to fragment either to $Ni^+ + n\text{-}C_4H_{10}$ reactants or to exothermic elimination products. The time during which $NiC_4H_{10}^+$ is accelerated by the extraction fields is about 2 μs. For $t_{ext} = 8$ μs, complexes that survive $t = 2-25$ μs after they are formed may fragment in the field-free drift region of the mass spectrometer.

Such metastable decay can be analyzed by applying a retarding potential[6] in the flight tube between the reaction zone and the detector, as shown in Figure 1 of ref 6. As compared with the usual time-of-flight mass spectrometer, the retarding potential device alters arrival times in a mass-dependent fashion. In the examples presented below, we are able to distinguish long-lived $NiC_4H_{10}^+$ complexes that survive the entire flight path intact, complexes that fragment in the field-free Region F1 (Figure 2, ref 6) before entering the retarding field, and complexes that fragment in the retarding device, Region R. Neutral fragments formed in F1 also create a distinguishable peak whose arrival time is insensitive to the retarding voltage V_r. By modeling the time-of-flight apparatus in one dimension using simple, piecewise constant electric fields, we are able to assign various fragment peaks from their arrival time behavior vs V_r as described in detail earlier.[6]

The experiment partitions the time t since complex formation into three overlapping windows. For $t_{ext} = 8$ μs, these are roughly $t = 2-10$ μs, $t = 6-24$ μs, and $t \geq 27$ μs. The time intervals are broadened and caused to overlap by the distribution of times between initiation of a collision and ion extraction. The earliest time window is the ion residence time in the source region, the time between the firing of the ionizing laser and the completion of ion acceleration, about $t_{ext} + 2$ μs. In this interval, we can measure an apparent total reaction cross section that includes as products long-lived complexes that survive extraction intact plus elimination products born prior to extraction. We measure the branching fractions of prompt elimination products and long-lived adducts averaged over the same time window by integrating the simple TOF-MS peaks. Those complexes that fragment to elimination products during the 2 μs ion acceleration time will appear as small tails on the proper elimination fragment ion and will mostly be included in the correct channel. We are blind to complexes that return to $Ni^+ + C_4H_{10}$ during this first time window, since the peak from those Ni^+ ions that never collide with *n*-butane is enormous on the scale of products.

The middle time window is the time spent by complexes in field-free Region F1, prior to interrogation by the retarding fields in Region R. For the typical extraction energy of 1280 eV, the flight time for $NiC_4H_{10}^+$ in F1 is 18 μs. For $t_{ext} = 8$ μs, complexes enter Region R with t in the range 20−28 μs after the initiation of the collision. The retarding field device integrates the decay kinetics of surviving complexes over a time window that varies from $t = 2-20$ μs (latest-born) to $t = 10-28$ μs (earliest-born). We refer to this as the 6−24 μs time window. Finally, we can measure the fraction of long-lived adducts that arrive at the detector intact as $NiC_4H_{10}^+$. On average, these complexes have survived 24 μs or longer.

III. Experimental Results

A. $Ni^+ + n\text{-}C_4H_{10}$, $E_t = 0.01$ eV. At 0.01 eV collision energy, the absolute reaction cross section is (40 ± 20)% of the Langevin cross section of 483 Å^2, as estimated from using 8.2 Å^3 for the polarizability of *n*-butane. Figure 1 shows the TOF mass spectrum for $t_{ext} = 6$ μs. Product branching fractions are 63 ± 5% $NiC_2H_4^+$ (C_2H_6 elimination, reaction 1b), < 1% $NiC_3H_6^+$ (CH_4 elimination, reaction 1c), 26 ± 2% $NiC_4H_8^+$ (H_2 elimination, reaction 1d) and 11 ± 4% intact $NiC_4H_{10}^+$ complexes (reaction 1a), as collected in Table 1 for $t_{ext} = 8$ μs. Within the reproducibility of the experimental branching fractions (~6%), the ratio $NiC_2H_4^+/NiC_4H_8^+$ is constant vs t_{ext}, strongly suggesting that both $NiC_2H_4^+$ and $NiC_4H_8^+$ have a common precursor and are formed on a similar time scale. Additionally, the $NiC_2H_4^+$ peak tails toward longer TOF at small reaction delays (Figure 1, inset). With a single-exponential decay model, the $NiC_2H_4^+$ peak (both narrow and tail components) is well fit with lifetime $\tau = 400 \pm 100$ ns.

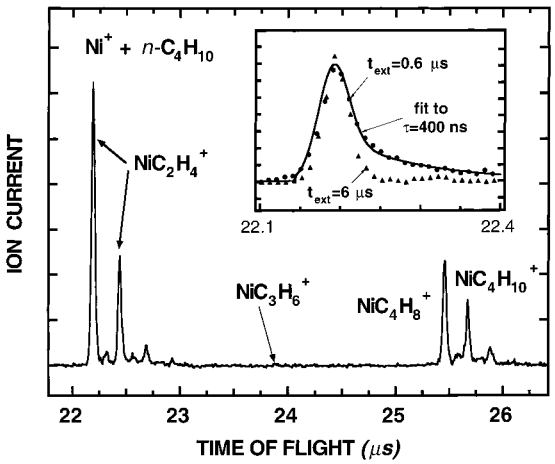

Figure 1. Time-of-flight mass spectrum product region for $Ni^+ + n\text{-}C_4H_{10}$ at nominal $E_t = 0.01$ eV, $t_{ext} = 6$ μs. Inset: comparison of $NiC_2H_4^+$ peak shape for $t_{ext} = 0.6$ μs (circles) and 6 μs (triangles, scaled to match at peak). Solid line is fit of tailing region to single-exponential model with $\tau = 400$ ns.

The presence of $NiC_4H_{10}^+$ in the TOF mass spectrum at $t_{ext} = 6$ μs indicates the existence of additional complexes with $\tau \gg 400$ ns. At $E_t = 0.01$ eV, these $NiC_4H_{10}^+$ complexes constitute roughly 11% of products, as estimated by decomposing the overlapping isotopic peaks. The slight tailing to shorter TOF on the predominantly $NiC_4H_{10}^+$ peaks (Figure 1) is due to fragmentation in the drift region of the TOF/MS and separation in the electric field at the detector. Retarding potential analysis is very difficult on the small adduct peak of Figure 1, so no quantitative data for $E_t = 0.01$ eV is included in Table 2. The long-lived $NiC_4H_{10}^+$ complexes dissociate to $Ni^+ + C_4H_{10}$, $NiC_2H_4^+ + C_2H_6$, and $NiC_3H_6^+ + CH_4$, or remain as intact adducts, in roughly equal amounts on the 16−24 μs time scale. No $NiC_4H_8^+$ was definitely observed, possibly due to the difficulty of separating this peak from interfering isotopes of the $NiC_4H_{10}^+$ complexes.

B. $Ni^+ + n\text{-}C_4H_{10}$, $E_t = 0.21$ eV. At 0.21 eV collision energy, the absolute reaction efficiency remains ~40%; the total reaction cross section has dropped essentially as $E_t^{-1/2}$ in accord with the Langevin model. The H_2 elimination and parent ion peak cluster is shown in the top trace of Figure 2, for $t_{ext} = 8$ μs. For $t_{ext} = 8$ μs, product branching fractions are the following: 55 ± 6% $NiC_2H_4^+$, <1% $NiC_3H_6^+$, 24 ± 3% $NiC_4H_8^+$, and 21 ± 5% long-lived $NiC_4H_{10}^+$ complexes (Table 1). The ratio $NiC_2H_4^+/NiC_4H_8^+$ varies slightly with t_{ext} , from 2.0 ± 0.1 at $t_{ext} = 1$ μs to 2.4 ± 0.2 at $t_{ext} = 8$ μs. The $NiC_2H_4^+$ peak again tails toward longer TOF. The narrow peak and tail again fit a single-exponential model with $\tau = 400 \pm 100$ ns, the same value obtained at $E_t = 0.01$ eV.

Long-lived $NiC_4H_{10}^+$ complexes definitely make up a larger proportion of prompt products at this collision energy (21 ± 5%) than at 0.01 eV (11 ± 4%). Although the total reaction cross section dropped as $E_t^{-1/2}$, a greater fraction of collisions

TABLE 1: Experimental and Model Branching Ratios, $t = 2-10$ μs after Collision[a]

	E_t (eV)	$NiC_2H_4^+ + C_2H_6$	$NiC_3H_6^+ + CH_4$	$NiC_4H_8^+ + H_2$	$NiC_4H_{10}^+$
expt	0.21	55 ± 5	<1	26 ± 3	19 ± 2
model	0.21	51	1	22	26
expt	0.01	63 ± 5	<1	26 ± 3	11 ± 2
model	0.01	74	<1	26	0
	E_t (eV)	$NiC_2D_4^+ + C_2D_6$	$NiC_3D_6^+ + CD_4$	$NiC_4D_8^+ + D_2$	$NiC_4D_{10}^+$
expt	0.21	37 ± 4	<1	10 ± 2	53 ± 5
model	0.21	46	<1	2	52

[a] Experimental data with $t_{ext} = 8$ μs. Adjusted kinetics model from Table 6 is integrated over appropriate time scale for comparison with experiment.

TABLE 2: Experimental and Model $NiC_4H_{10}^+$ Fragmentation Pattern, $t = 16-24$ μs after Collision[a]

	E_t (eV)	$NiC_2H_4^+ + C_2H_6$	$NiC_3H_6^+ + CH_4$	$NiC_4H_8^+ + H_2$	$Ni^+ + C_4H_{10}$
expt	0.21	23 ± 5	3 ± 3	<1	74 ± 10
model	0.21	12	0	4	84
	E_t (eV)	$NiC_2D_4^+ + C_2D_6$	$NiC_3D_6^+ + CD_4$	$NiC_4D_8^+ + D_2$	$Ni^+ + C_4D_{10}$
expt	0.21	50 ± 30	<1	<1	50 ± 30
model	0.21	78	<1	1	21

[a] Experiment with $t_{ext} = 8$ μs. Adjusted kinetics model from Table 4 is integrated over appropriate time scale for comparison with experiment.

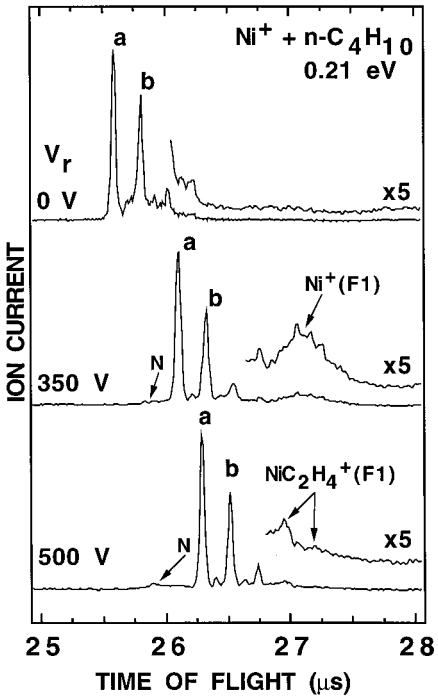

Figure 2. Product mass spectra for $Ni^+ + n\text{-}C_4H_{10}$ vs retarding potential V_r as shown. Peak labeled *a* is due to prompt $^{58}NiC_4H_8^+$; *b* is a blend of $^{60}NiC_4H_8^+$ and $^{58}NiC_4H_{10}^+$; *N* is due to fast neutrals arising from delayed fragmentation. As V_r increases, broad peaks due to fragmentation in the field-free flight region F1 move to later times than the sharp peaks due to intact products. They broaden because the Wiley−McLarin space-focusing condition no longer holds.

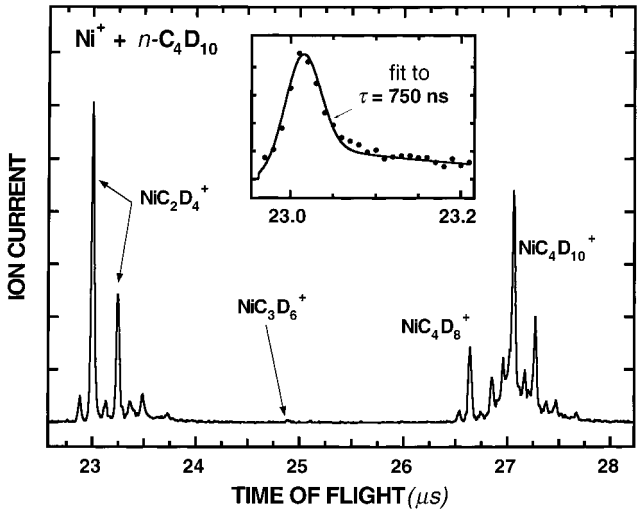

Figure 3. Time-of-flight mass spectrum product region for $Ni^+ + n\text{-}C_4D_{10}$ at $E_t = 0.21$ eV, $t_{ext} = 6$ μs. Inset: $NiC_2D_4^+$ peak shape for $t_{ext} = 0.6$ μs (circles). Solid line is fit of tailing region to single-exponential model with $\tau = 750$ ns.

at 0.21 eV results in $NiC_4H_{10}^+$ complexes. With the possible exception of $NiC_3H_6^+$ (which is not detected), the metastable decay branching fractions as revealed by retarding field analysis (Figure 2, Table 2) are experimentally similar at the two energies studied. Dissociation to Ni^+ accounts for 46 ± 20%, $NiC_2H_4^+$ accounts for 14 ± 13%, $NiC_3H_6^+$ for 2 ± 2%, and intact $NiC_4H_{10}^+$ 38 ± 18%. No $NiC_4H_8^+$ was detected.

C. $Ni^+ + n\text{-}C_4D_{10}$, $E_t = 0.21$ eV. The reaction with *n*-butane-d_{10} was studied at 0.21 eV collision energy, although absolute reaction cross sections were not measured. The product region of the TOF mass spectrum for $t_{ext} = 8$ μs is shown in Figure 3, along with the tail on the C_2D_6 elimination peak. As with *n*-butane-h_{10}, there is virtually no methane elimination product ($NiC_3D_6^+$, reaction 1b). The ethane elimination product, $NiC_2D_4^+$ (reaction 1a), is again prominent. In contrast, the relative abundance of hydrogen elimination product, $NiC_4D_8^+ + D_2$ (reaction 1c), is considerably diminished. Additionally, the relative amount of intact parent ion, $NiC_4D_{10}^+$ (reaction 1d), has markedly increased, with more noticeable tailing toward shorter TOF. Prompt branching fractions vary slightly with t_{ext}. At $t_{ext} = 860$ ns, branching fractions are $NiC_2D_4^+$ 31 ± 1%, $NiC_3D_6^+$ 1 ± 2%, $NiC_4D_8^+$ 8 ± 1%, and intact $NiC_4D_{10}^+$ parents 60 ± 2%. At $t_{ext} = 8$ μs (Table 1), the branching fractions are 37 ± 5%, <1%, 10 ± 2%, and 53 ± 7%, respectively. However, the ratio $NiC_2D_4^+/NiC_4D_8^+$ is constant within experimental error vs t_{ext}. Once again, this suggests a common intermediate and a similar time scale for hydrogen and ethane elimination.

As for *n*-butane-h_{10}, the $^{58}NiC_2D_4^+$ peak from *n*-butane-d_{10} noticeably tails to longer TOF for small reaction delays (Figure 3, inset). Both the narrow component and the tail are reasonably well fit by a single-exponential decay with lifetime $\tau = 750 \pm 100$ ns, significantly longer than the $NiC_4H_{10}^+$ lifetime of 400

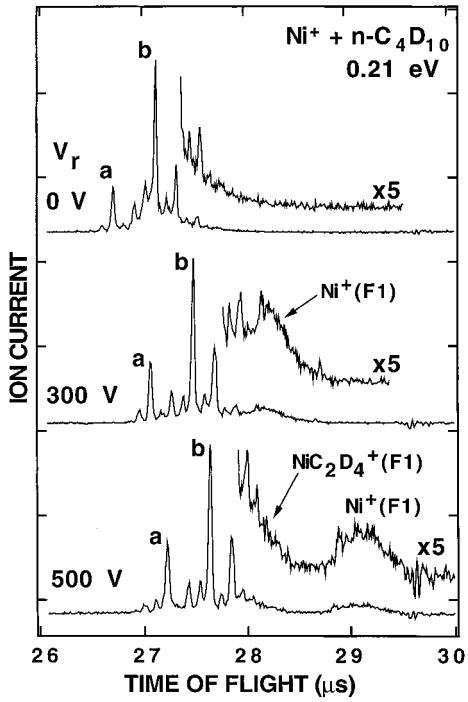

Figure 4. Product mass spectra for $Ni^+ + n\text{-}C_4D_{10}$ vs retarding potential V_r as shown. Peak labeled *a* is due to prompt $^{58}NiC_4D_8^+$; *b* is predominantly $^{58}NiC_4D_{10}^+$.

$\pm$ 100 ns at the same collision energy. Fits to several such traces consistently underestimate the experimental data in the region just beyond the narrow peak (at 23.05−23.10 μs TOF), strongly suggesting nonexponential decay. Fits to the *n*-butane-h_{10} peaks were consistently better over the entire curve.

The large proportion of intact $NiC_4D_{10}^+$ parents cannot be explained on the basis of a single-exponential decay with 750 ns lifetime, since less than 1% of the products would remain intact $NiC_4D_{10}^+$ parents after 8 μs, while 53% $NiC_4D_{10}^+$ is observed. Retarding field mass spectra were collected for V_r between 300 and 1000 V (Figure 4). Analysis shows that the 22 $\pm$ 5% of the $NiC_4D_{10}^+$ parent ions decay to Ni^+, 22 $\pm$ 6% decay to $NiC_2D_4^+$, and that 56 $\pm$ 12% remain as $NiC_4D_{10}^+$ (Table 2). No $NiC_3D_6^+$ or $NiC_4D_8^+$ were detected.

IV. Electronic Structure Calculations

The electronic structure calculations from which we build the rate model were carried out as described earlier for $Ni^+ + C_3H_8$.[7] First, stationary points on the ground-state (doublet) $NiC_4H_{10}^+$ potential energy surface are located using B3LYP,[1,20] a density functional theory (DFT) based on hybrid functionals. In the B3LYP geometry optimizations the LANL2DZ basis set of the *Gaussian-94* program[21] is used. For the nickel atom this includes a nonrelativistic effective core potential (ECP) according to Hay and Wadt[22] together with a valence basis set of essentially double-ζ quality including a diffuse 3d function. The other atoms have a standard double-ζ basis set. In each structure obtained in this way (minimum or transition state), an energy calculation is performed at the B3LYP level using the large basis set 6-311+G(2d,2p) in the *Gaussian-94* program. This includes the Wachters[23] all-electron basis on nickel, two sets of polarization functions on all atoms including two f-sets on nickel, and also diffuse functions. All relative energies reported are based on the results for this large basis.

Zero-point vibrational energies were determined for all stationary points as follows. At each optimized stationary point the force-constant matrix was calculated to determine the character of the stationary points (minima or transition states), and also to evaluate the zero-point vibrational energy corrections, which are included in all relative energies. The calculations of the force-constants were performed at the B3LYP level using essentially double-ζ quality basis sets. For the nickel atom the Wachters all-electron basis set was used. Since the basis used in the force calculations is not exactly the same as the basis used for the geometry optimizations, the separation between overall rotation, translation, and internal motion is imperfect, which causes the smallest vibrational frequencies (below 100 cm^{-1}) to be uncertain.

B3LYP often overestimates the stability of atomic $3d^x$ configurations relative to $3d^{x-1}4s$. For Ni^+, this is a very mild effect. The energy difference between the$3d^84s(^4F)$ excited state and the $3d^9(^2D)$ ground state as calculated in the present study is 28.6 kcal/mol, only 3.7 kcal/mol higher than the experimental difference in $(2J_{el} + 1)$-weighted energies of 24.9kcal/mol. Ricca andBaushlicher[24] have suggested a scheme for correcting for errors in the atomic spectra when calculating the energetics of molecular species by interpolation between atomic asymptotes based on the 3d population of the metal atom in the molecule. We have followed their scheme in this work, but the largest resulting correction is only 1.2 kcal/mol.

The B3LYP energetic results are summarized in Table 3. The names of potential wells and transition states refer to the kinetics scheme and reaction paths shown in Figures 5−8. For each species, we give the energy relative to ground state ($3d^{9,2}D$) reactants, corrected for differential zero-point energy and for

TABLE 3: Calculated Reaction Path Energetics for $Ni^+ + C_4H_{10}$ and $Ni^+ + C_4D_{10}$ from Density Functional Theory (B3LYP)[a]

species[a]	ΔE_H	ΔE_D
$Ni^+ + C_4H_{10}$	0	0
$Ni(C_4H_{10})^+$	−32.0	−31.9
TS_{CC} (central)	−13.6	−13.2
$Ni(C_2H_5)(C_2H_5)^+$ [b]	−22.6	−22.2
$MCTS_{C_2H_6}$	−10.9	−9.7
$Ni(C_2H_4)(C_2H_6)^+$ [b]	−48.0	−47.5
$Ni(C_2H_4)^+ + C_2H_6$ [c]	−34.5	−34.1
$MCTS_{H_2}$	−5.7	−3.8
$Ni(C_2H_4)_2(H_2)^+$ [b]	−42.1	−40.2
$Ni(C_2H_4)_2^+ + H_2$ [d]	−39.3	−36.8
TS_{CC} (terminal)	−14.8	−14.4
$Ni(CH_3)(C_3H_7)^+$	−23.4	−22.9
$MCTS_{CH_4}$	−2.5	+1.1
$Ni(C_3H_6)(CH_4)^+$	−58.1	−57.4
$Ni(C_3H_6)^+ + CH_4$	−38.8	−38.1
$TS_{CH}(1°)$	−12.4	−9.4
$Ni(H)(n\text{-}C_4H_9)^+$	−12.8	−11.3
$MCTS_{H_2}(1°)$	+9.1	+11.0
$Ni(1\text{-butene})(H_2)^+$	−40.4	−38.9
$Ni(1\text{-butene})^+ + H_2$	−28.2	−25.9
$MCTS_{C_2H_6}(1°)$	−0.2	+3.5
$TS_{CH}(2°)$	−14.2	−13.1
$Ni(H)(iso\text{-}C_4H_9)^+$	−15.9	−15.0
$MCTS_{H_2}(2°)$	−0.1	+1.6
$Ni(2\text{-butene})(H_2)^+$	−44.5	−42.9
$Ni(2\text{-butene})^+ + H_2$	−31.4	−29.0

[a] See text for theoretical procedure. Energies in kcal/mol relative to ground-state reactants and including differential zero-point energy corrections. ΔE_H refers to $Ni^+ + C_4H_{10}$; ΔE_D refers to $Ni^+ + C_4D_{10}$. Most species identified in Figures 5−8. Notation (1°) and (2°) refers to initial insertion into primary or secondary CH bond, respectively. [b] Geometry optimization incomplete; these complexes includes one or two imaginary frequencies in the range 12i−162i cm^{-1}. They do not enter the calculated rates. [c] Experimental estimate of exothermicity: −22 $\pm$ 4 kcal/mol (refs 25, 26). [d] Experimental estimate of exothermicity: −32 $\pm$ 7 kcal/mol (refs 25, 26).

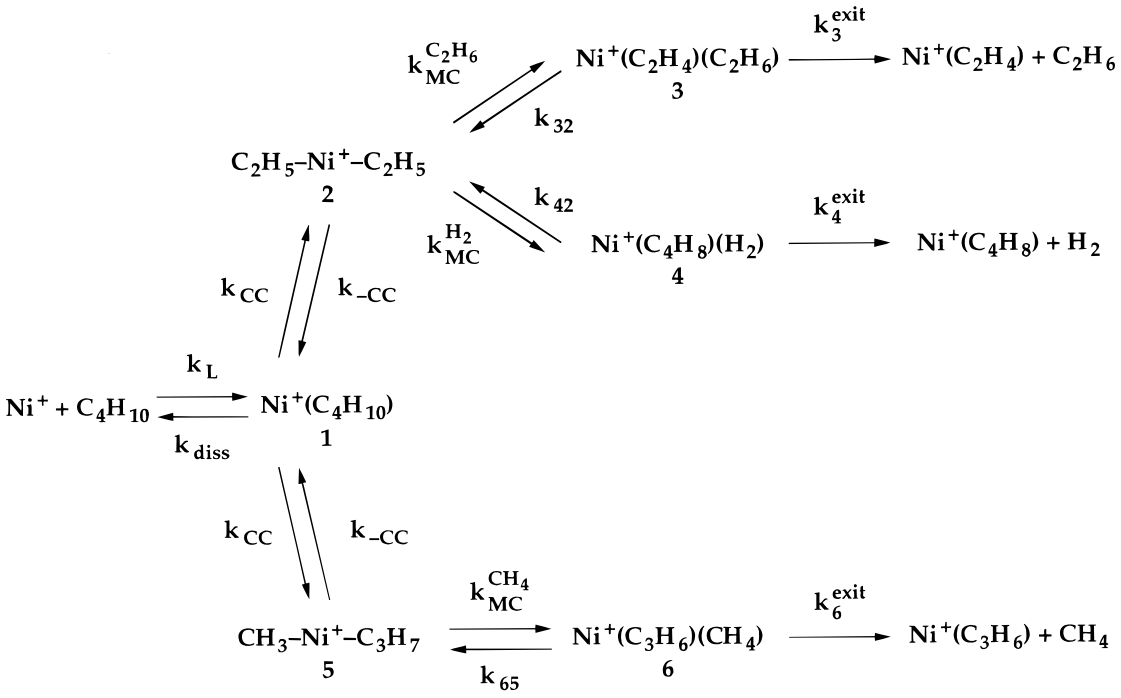

Figure 5. Kinetics scheme.

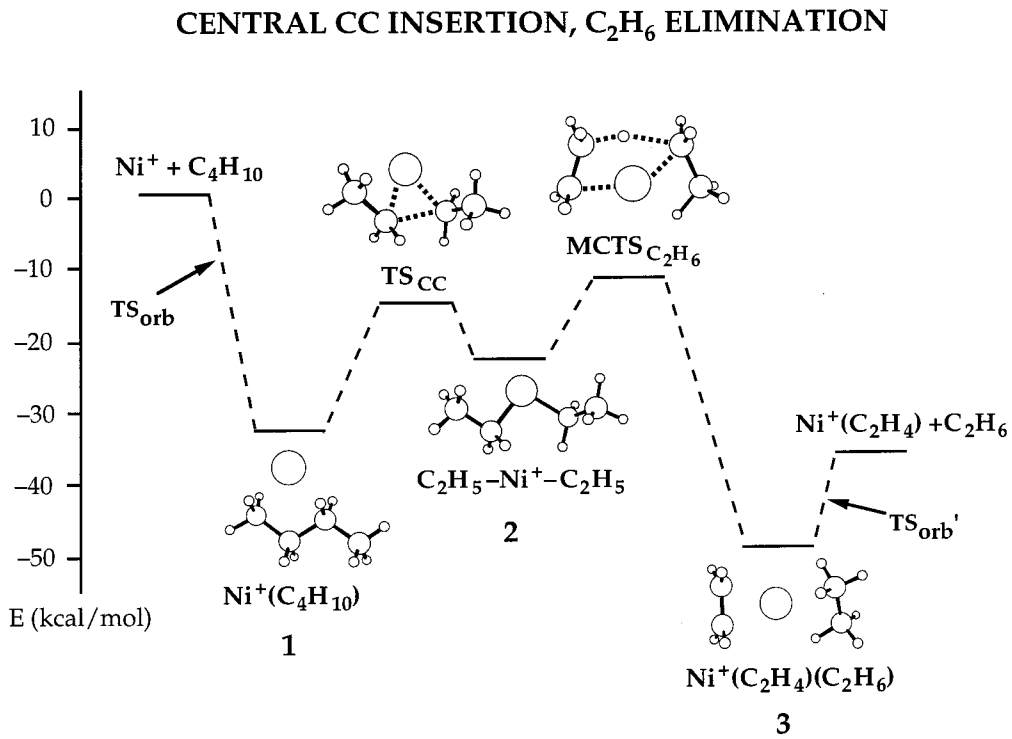

Figure 6. Reaction pathway to $NiC_2H_4^+ + C_2H_6$ elimination products; energies as calculated by B3LYP theory (Table 3), not adjusted to agree with experiment.

3d orbital occupancy as described above. Results for both $Ni^+ + n\text{-}C_4H_{10}$ and $Ni^+ + n\text{-}C_4D_{10}$ are given. Harmonic vibrational frequencies and rotational constants at the key stationary points (Tables 4 and 5) will be used directly in the statistical rate calculations.

The B3LYP calculations find three exothermic reaction channels, C_2H_6, H_2, and CH_4, consistent with experimental observations at low collision energies. The calculated gas-phase exothermicity for the dominant elimination process $Ni^+ + C_4H_{10} \rightarrow Ni(C_2H_4)^+ + C_2H_6$ is 34.5 kcal/mol, compared with the estimate of 22 ± 4 kcal/mol based on experimental bond energies.[25,26] The B3LYP exothermicity for $Ni^+ + C_4H_{10} \rightarrow Ni(C_2H_4)_2^+ + H_2$ is 39.3 kcal/mol, compared with the experimental estimate of 32 ± 7 kcal/mol. The discrepancies are substantial.

In the statistical rate modeling, the energies of the multicenter transition states (MCTSs) determine product branching fractions, since they are by far the highest potential energy points on each reaction path. The geometries of three key multicenter transition states are shown in Figure 9. The relative energies of the MCTSs along the lowest energy pathways to the three observed elimination products lie in accord with the experimental

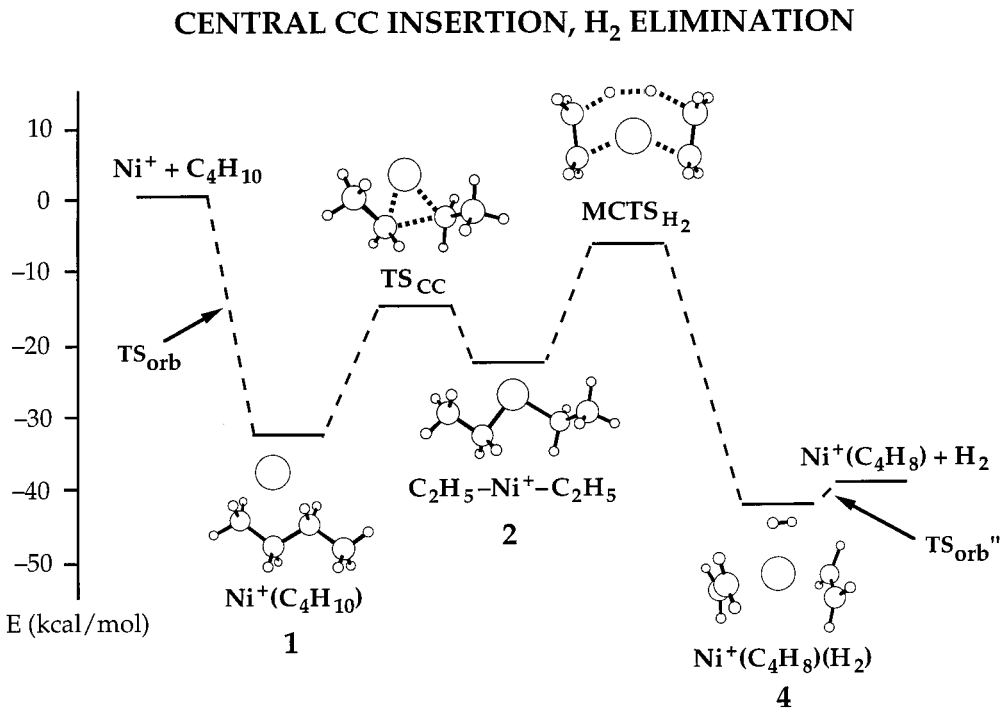

Figure 7. Reaction pathway to $NiC_4H_8^+ + H_2$ elimination products; energies as calculated by B3LYP theory (Table 3), not adjusted.

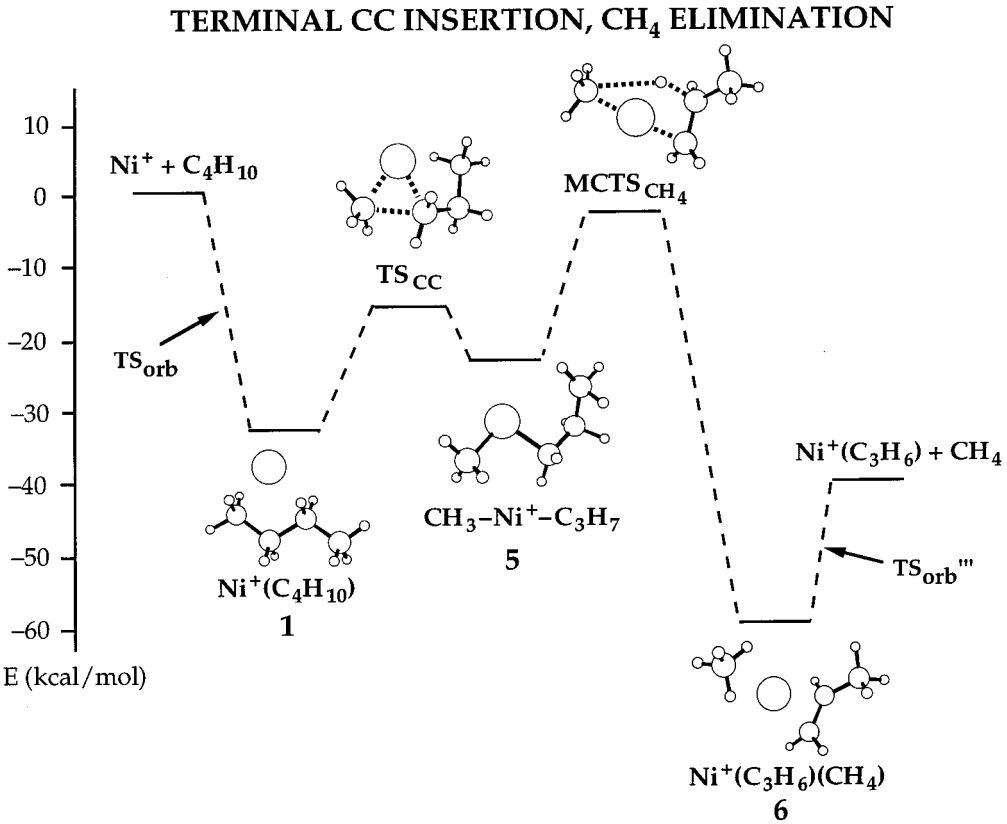

Figure 8. Reaction pathway to $NiC_3H_6^+ + CH_4$ elimination products; energies as calculated by B3LYP theory (Table 3), not adjusted.

branching: $MCTS_{C_2H_6}$ at −10.9 kcal/mol, $MCTS_{H_2}$ at −5.7 kcal/mol, and $MCTS_{CH_4}$ at −2.5 kcal/mol. These MCTSs were found by trial and error using previous work as a general guide. The Ni^+/C_4H_{10} system is sufficiently large that it was not feasible to follow the intrinsic reaction path downward in energy from each MCTS to confirm which two potential minima are connected by each transition state. Nor is it possible to guarantee that we have found all the important low-lying MCTSs that might contribute to the actual reaction, but the overall results show a satisfying consistency with previous work on other reactions.

The lowest of these barriers is $MCTS_{C_2H_6}$, arising from insertion into the central CC bond (the weakest bond in the molecule) and migration of a single β-hydrogen to the metal center. The alternative pathway to ethane elimination, which involves initial insertion into a primary CH bond followed by

TABLE 4: Vibrational Frequencies (cm^{-1}) Used in RRKM Calculations[a]

complex (**1**)	$MCTS_{C_2H_6}$	$MCTS_{H_2}$	$MCTS_{CH_4}$
3164	3257	3266	3231
3157	3242	3256	3209
3143	3216	3242	3173
3126	3196	3229	3143
3081	3140	3148	3121
3061	3139	3137	3118
3028	3113	3132	3114
2996	3106	3124	3055
2667	2439	1693	3004
2532	1754	1594	1776
1582	1561	1521	1523
1522	1508	1513	1514
1520	1494	1470	1494
1511	1468	1468	1452
1500	1466	1272	1448
1479	1409	1266	1404
1452	1319	1244	1402
1402	1291	1224	1285
1369	1183	1190	1235
1341	1174	1162	1177
1314	1158	1157	1133
1293	1131	1081	1062
1210	1045	992	981
1141	977	969	969
1085	927	865	906
1010	923	855	706
985	859	753	685
974	750	697	596
861	634	571	560
836	489	501	502
762	464	477	409
481	451	463	389
377	403	412	309
256	312	389	199
234	251	302	166
191	175	117	116
182	102	104	89
134	26[b]	95	57
113			

[a] See Figures 5−8 for species. [b] This very low frequency is uncertain due to technical factors (see details in ref 7). This 26 cm^{-1} mode was replaced by a 100 cm^{-1} in all calculations. See text.

TABLE 5: Key Rotational Constants (cm^{-1}) Used in RRKM Calculations[a]

complex (**1**)	$MCTS_{C_2H_6}$	$MCTS_{H_2}$	$MCTS_{CH_4}$
0.157	0.312	0.353	0.233
0.073	0.077	0.072	0.064
0.052	0.065	0.063	0.058

[a] See Figures 5−8 for species. The *B* and *C* rotational constants are averaged in the actual model calculations.

β-ethyl migration over what we label $MCTS_{C_2H_6}(1°)$, lies 10 kcal/mol higher in energy. This is consistent with previous calculations on $Fe^+ + C_3H_8$,[27] $Co^+ + C_3H_8$,[28] and $Ni^+ + C_3H_8$,[7] which always find pathways involving β-alkyl migrations to the metal unfavorable relative to β-hydrogen migrations.

The lowest energy pathway to H_2 elimination passes over $MCTS_{H_2}$ at −5.7 kcal/mol; it involves simultaneous migration of two β-hydrogens, resulting in the bis(ethylene) complex **4**. This is a novel MCTS that lacks an analogue in the propane case. In the dehydrogenation of butane by Ni^+, evidence from several experiments supports highly specific 1,4-H_2 elimination,[8,29,30] consistent with this B3LYP pathway. The B3LYP calculations were unable to locate stable minima of the form $Ni^+(H)(C_2H_5)(C_2H_4)$ or $Ni^+(H_2)(C_2H_4)_2$. Such minima were invoked in earlier mechanisms.[29−32] Following primary CH insertion, we do find an H_2 elimination pathway involving

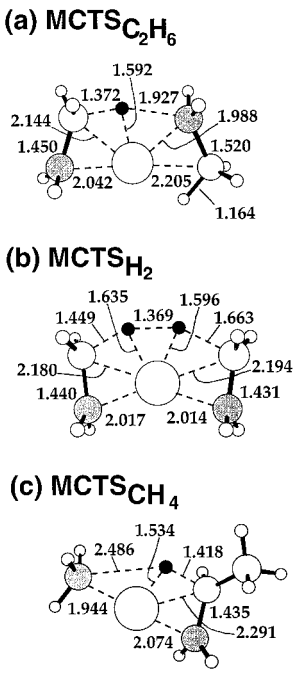

Figure 9. Key multicenter transition states (MCTSs) from B3LYP theory. Interatomic distances in Å. Shaded carbon atoms are those into which the Ni^+ ion originally inserted. Black H atoms are migrating to form new bonds.

β-hydrogen migration via $MCTS_{H_2}(1°)$, but its energy is +9.1 kcal/mol, far above $MCTS_{H_2}$. A lower energy route is initial insertion into a (weaker) secondary CH bond and passage over $MCTS_{H_2}(2°)$, whose calculated energy is −0.1 kcal/mol. Consistent with the B3LYP energetics, we assume in the rate modeling that the double β-hydrogen migration over $MCTS_{H_2}$ is the only important path to H_2 elimination at low kinetic energy.

For methane elimination, the lowest energy pathway involves initial insertion into a terminal CC bond followed by $MCTS_{CH_4}$ at −2.5 kcal/mol. A completely analogous route to CH_4 elimination from $Ni^+ + C_3H_8$ was found at +3.1 kcal/mol in earlier work. In $Ni^+ + C_3H_8$ this is the dominant reaction path,[7] whereas in $Ni^+ + n\text{-}C_4H_{10}$ the other pathways involving central CC insertion lie much lower in energy and render CH_4 a minor channel.

In our kinetics model, the initial $Ni(C_4H_{10})^+$ complex **1** is assumed to be the common precursor to both the central and terminal CC insertion paths. In **1**, Ni^+ is in close proximity to a primary and a secondary carbon of *trans*-butane. B3LYP finds an energetically more favored structure (−1.3 kcal/mol relative to **1**) in which Ni^+ is in close proximity to two primary carbons of *gauche*-butane. In addition, B3LYP finds two additional energetically less favored structures (+0.6 kcal/mol and +4.0 kcal/mol relative to **1**). It is plausible that different minima might be the immediate precursors to different elimination paths. Our assumption in the modeling is that all such complex structures interconvert rapidly over low barriers on the time scale of bond insertion and rearrangement, so that they are well represented by a single kinetic species.

V. Statistical Rate Model

A. Construction of RRKM Model. The statistical rate model is built in the same spirit as our earlier effort for $Ni^+ + C_3H_8$.[7] Most of the details are not repeated here. We assume the B3LYP calculations have all the important low-energy reaction paths and determined the relative energetics well enough to reliably

indicate the dominant pathway to each observed elimination product, C_2H_6, H_2, and CH_4. The kinetics model of Figure 5 includes the B3LYP stationary points (potential wells and transition states) along three parallel paths leading away from a common long-lived $Ni^+(C_4H_{10})$ ion-induced dipole complex **1**. We assume such complexes are formed at the Langevin rate constant k_L and subsequently decay into four parallel channels: dissociation back to reactants (k_{diss}); central CC bond insertion to intermediate **2**, leading to eventual C_2H_6 elimination ($k_{C_2H_6}$) and H_2 elimination (k_{H_2}); and terminal CC bond insertion to intermediate **5**, leading to eventual CH_4 elimination (k_{CH_4}). Figures 6−8 show key intermediates and transition states along the three postulated elimination paths. There is also a deep ion-induced dipole complex for each exit channel, **3** for the C_2H_6 channel, **4** for the H_2 channel, and **6** for the CH_4 elimination channel. Other paths lie at substantially higher energy (Table 3) and are assumed not to contribute at the low collision energies of interest here. In particular, we neglect the next lowest energy path to H_2 elimination involving secondary CH insertion and $MCTS_{H_2}$, which lies 5.6 kcal/mol above $MCTS_{H_2}$, nearly at the reactants' asymptote. Still a third pathway to H_2 over $MCTS_{H_2}$-(1°) lies 14.8 kcal/mol above $MCTS_{H_2}$ and is also neglected. These latter two MCTSs can be ruled out at low energy on experimental grounds as well, since they are inconsistent with isotopic labeling studies that indicate exclusive 1,4 H_2 elimination.[29,30]

To calculate each of the microcanonical rates $k_i(E,J)$ in Figure 5, we use RRKM theory. In doing so, we implicitly assume that reaction occurs on a single potential energy surface, that intramolecular energy redistribution is instantaneous on the time scale of each reaction step, and that, in the language of classical mechanics, there are no "re-crossing" trajectories that pass forward and then backward across the transition state. The distribution of J is calculated from the Langevin capture cross section[33] by assuming that only orbital angular momentum contributes to J of the complex. Exactly as before in $Ni^+ + C_3H_8$, the energetics gleaned from the B3LYP calculations (Figures 6−8) place each parallel elimination channel in a simple steady-state limit. The overall decay of the complex for fixed (E,J) becomes exponential with the rate constant:

$$k_{tot}(E,J) = k_{diss}(E,J) + k_{C_2H_6}(E,J) + k_{H_2}(E,J) + k_{CH_4}(E,J) \quad (2)$$

Each of the three elimination rates is obtained by applying the steady-state approximation to the appropriate short-lived intermediate, either **2** or **5**. A simplification described elsewhere[7] leads to the following expression, for example:

$$k_{C_2H_6}(E,J) = W^{\dagger}(MCTS_{C_2H_6})/h\rho(\mathbf{1}) \quad (3)$$

Here $W^{\dagger}$ is the sum of states at the MCTS and $\rho(\mathbf{1})$ is the density of states at the complex **1**. Analogous expressions hold for k_{CH_4} and k_{H_2}. To match experiment, we will adjust the B3LYP barrier heights downward by several kcal/mol each. This places the adjusted energy of $MCTS_{C_2H_6}$ and of $MCTS_{H_2}$ within 1−2 kcal/mol of the unadjusted energy of the preceding TS_{CC}(central). If this were strictly true, the expression in eq 3 and its analogues for the other rates would not be correct. However, we expect that B3LYP also overestimates the energy of TS_{CC}(central), so the simplified expressions are likely valid in actual fact.

The complex **1** and the entrance channel orbiting transition state TS_{orb} have soft degrees of freedom corresponding to the $Ni^+-C_4H_{10}$ stretch and two soft bending motions, plus two methyl torsions and one CH_2-CH_2 torsion. As in our treatment of the $Ni^+ + C_3H_8$ reaction, the two soft bends are treated as harmonic vibrations in **1** and as a two-dimensional free internal rotation of C_4H_{10} relative to Ni^+ in TS_{orb}. In the complex **1**, the three torsions are modeled as free internal rotations since the internal energy far exceeds the typical barrier heights of 3 kcal/mol for these torsions. In contrast, in TS_{orb} we treat the three torsions as harmonic vibrations since the internal energy is low.

The B3LYP calculations found one unusually low vibrational frequency of 26 cm^{-1} in $MCTS_{C_2H_6}$. This is a complicated mode; it is not purely internal methyl rotation. As discussed above, frequencies below about 100 cm^{-1} are unreliable. We tested the effect of replacing 26 cm^{-1} with 100 cm^{-1}. Use of the 100 cm^{-1} mode decreases the density of states at $MCTS_{C_2H_6}$ moderately, which in turn causes us to lower our estimate of the energy of this barrier by about 2 kcal/mol. We kept the 100 cm^{-1} mode in all subsequent calculations. The B3LYP calculations also found the low-frequency vibration of 57 cm^{-1} in $MCTS_{CH_4}$. This mode corresponds to internal rotation of a methyl group loosely attached to Ni^+. In this case, we kept the 57 cm^{-1} vibration in all subsequent calculations. The microscopic rates k_{diss}, $k_{C_2H_6}$, k_{CH_4}, and k_{H_2} calculated using state densities without symmetry numbers must be multiplied by appropriate symmetry numbers[13,34] to incorporate the reaction path degeneracy, as before.

B. Adjustment of MCTS Energies. In the $Ni^+ + C_3H_8$ case,[7] the key MCTSs lie quite high in energy relative to reactants so that the fastest time scale for complex decay was set by k_{diss}. Our strategy was to adjust the modeling of the complex and the loose transition state TS_{orb} to match the experimental time scale and then independently adjust the MCTS energies to fit the observed elimination branching. For $Ni^+ + n$-C_4H_{10}, the key MCTSs lie much lower in energy relative to reactants so that the time scale of the decay is dominated by $k_{C_2H_6}$ rather than k_{diss}. In this case, the data themselves do not adequately constrain the treatment of k_{diss}, so we use the same treatment that was successful for $Ni^+ + C_3H_8$. The energy of the complex **1** was initially fixed at the B3LYP value of −32.0 kcal/mol. We then adjusted $MCTS_{C_2H_6}$, the barrier for the dominant C_2H_6 elimination channel, to match the experimental decay time scale at $E_t = 0.21$ eV. The relative energies of $MCTS_{H_2}$ and $MCTS_{CH_4}$ were then adjusted to match the product branching at the same energy. The model is then used to predict the results for $Ni^+ + n$-C_4H_{10} at nominal $E_t = 0.01$ eV and for $Ni^+ + n$-C_4D_{10} at 0.21 eV. We find that the data constrain the energy of the complex **1** to lie within 1−2 kcal/mol of −32.0 kcal/mol. The modeling of $Ni^+ + n$-C_4H_{10} is thus satisfyingly consistent with the treatment that succeeded for $Ni^+ + C_3H_8$.

Using the B3LYP energetics in Table 3 without adjustment gives $k_{C_2H_6} = 4 \times 10^6$ s^{-1}, somewhat too slow compared with the fastest experimental elimination time scale of 100 ns or less. To make the fastest $k_{C_2H_6}$ rate on the order of 10^7 s^{-1}, it is necessary to lower $MCTS_{C_2H_6}$ by 3.1 kcal/mol from the B3LYP value of −10.9 kcal/mol. Without adjustment, the B3LYP energetics predict 99% C_2H_6 elimination and only 1% H_2 elimination at $E_t = 0.21$ eV, in disagreement with experiment. To fit the 2:1 C_2H_6:H_2 elimination branching ratio from our experiment, it is then necessary to lower $MCTS_{H_2}$ by 6.8 kcal/mol from the B3LYP value of −5.7 kcal/mol. Its energy becomes −12.5 kcal/mol, quite close to the adjusted energy of $MCTS_{C_2H_6}$. If we lower $MCTS_{H_2}$ by only 3.1 kcal/mol so that the energy difference between the two MCTSs remains the same as given by B3LYP, then the C_2H_6:H_2 elimination branching ratio increases to 99:1, far in excess of experimental value of 2:1. If we assume that only the 25% of J's that cross $MCTS_{H_2}$

TABLE 6: Key Stationary Point Energetics from B3LYP and for Adjusted Model[a]

species	B3LYP	adjusted model
$NiC_4H_{10}^+$	−32.0	−32.0
$MCTS_{C_2H_6}$	−10.9	−14.0, −12.9[b]
$MCTS_{H_2}$	−5.7	−12.5
$MCTS_{CH_4}$	−2.5	−7.0, −6.6[b]

[a] Energetics in kcal/mol relative to reactants, including ΔZPE_H corrections appropriate to $Ni^+ + C_4H_{10}$. [b] Two different energies were equally successful in fitting the data, depending on the detailed treatment of soft degrees of freedom; see text for details. Overall, we estimate that the data constrain the three MCTS energies to lie within ±3 kcal/mol of the values −14.0, −12.5, and −7.0 kcal/mol for $MCTS_{C_2H_6}$, $MCTS_{H_2}$, and $MCTS_{CH_4}$, respectively.

make H_2 due to exit-channel centrifugal effects,[7,35] as discussed further below, we have to lower $MCTS_{H_2}$ further from −12.5 to −18.7 kcal/mol, placing $MCTS_{H_2}$ lower than $MCTS_{C_2H_6}$ by 4.7 kcal/mol. If, in reality, another higher energy pathway contributes to the H_2 product at low E_t, we have undoubtedly lowered $MCTS_{H_2}$ too much in the model. However, if we assume that B3LYP provides fairly accurate relative energies of $MCTS_{H_2}$ and $MCTS_{H_2}(2°)$, then the rate modeling indicates that the latter will not contribute significantly to H_2 production at the energies studied here. Finally, to fit the observed 1% CH_4 elimination, it is necessary to lower the $MCTS_{CH_4}$ from −2.5 to −7.0 kcal/mol.

The preferred model is described under the heading "Adjusted Model" in Table 6. The dual entry for the energy of $MCTS_{C_2H_6}$, −14.0, and −12.9 kcal/mol, shows two different values which can fit the time-dependent branching fractions. If the methyl torsion of 251 cm^{-1} is treated as vibration, the energy of $MCTS_{C_2H_6}$ must be lowered to −14.0 kcal/mol. Alternatively, if the methyl torsion is treated as free internal rotation, the energy must be increased to −12.9 kcal/mol. This places $MCTS_{C_2H_6}$ within 1−2 kcal/mol of the CC insertion TS. We have checked that even with this adjustment the sum of states at $MCTS_{C_2H_6}$ dominates that at TS_{CC}, which ensures the validity of the simplification of the rate expression in eq 3. Similarly, the dual entry for the energy of $MCTS_{CH_4}$ in Table 4, −7.0 and −6.6 kcal/mol, is determined by modeling the two methyl torsions of 57 and 199 cm^{-1} in two different ways, as vibrations or internal rotations. $MCTS_{H_2}$ does not have methyl torsion, resulting in the single entry for the energy in Table 4. We have exercised the model extensively by using various combinations of assumption, but is not easy to estimate quantitatively how tightly the data constrain the MCTS energies. Clearly these energies must move downward compared with B3LYP results. As a rough estimate, we believe that the three MCTS energies lie within ±3 kcal/mol of the values −14.0, −12.5, and −7.0 kcal/mol for $MCTS_{C_2H_6}$, $MCTS_{H_2}$, and $MCTS_{CH_4}$, respectively. If one MCTS moves up or down, the other two should follow, since the chemical branching is very sensitive to relative barrier heights.

C. Comparison of Adjusted Model Results with Experiment. *1. Time-Dependent Branching Fractions at $E_t = 0.21$ eV.* In Figure 10 we compare the J dependence of the four parallel decay rates k_{diss}, $k_{C_2H_6}$, k_{CH_4}, and k_{H_2} for the adjusted model at $E_t = 0.21$ eV. These are summed to form the overall complex decay rate k_{tot} as in eq 2. Despite well-defined initial kinetic energy and internal energy, the model finds the distribution of k_{tot} to include substantial contributions from rates varying a factor of 500, from 10^5 to 5×10^7 s^{-1}. We believe this is the qualitative explanation for the range of apparent time scales for breakup of the collision complexes observed in the experiments.

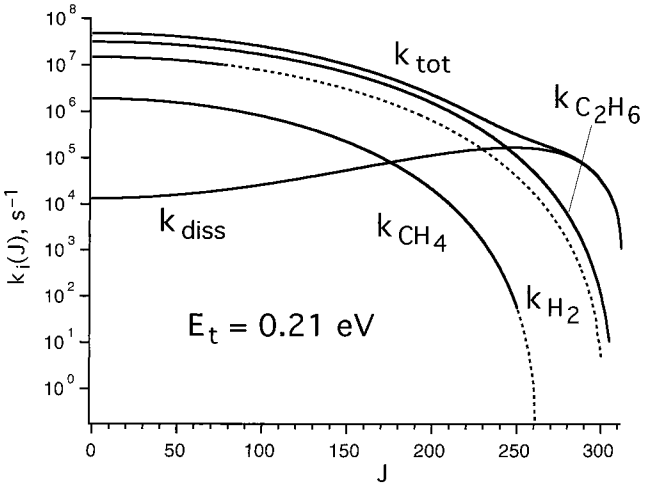

Figure 10. Microscopic parallel decay rates $k_i(E,J)$ for adjusted model of $Ni^+ + n\text{-}C_4H_{10}$ (Table 6) at $E_t = 0.21$ eV as a function of J. Dashed lines are products that would be cut off by exit channel centrifugal effects under the strong assumption $l = l'$ for H_2 or $l = l'''$ for CH_4, as described in text.

We use the distributions in Figure 10 to construct properly weighted ($P(J) = 2J/J_{max}^2$) time-dependent branching fractions for comparison with experiment as before.[7] Elimination of C_2H_6, CH_4, and H_2 occurs on the earliest time scale primarily from complexes formed at low J (small impact parameter). Complexes formed at very high J (large impact parameter) dissociate more slowly and primarily back to Ni^+, in qualitative agreement with the retarding field experiments. At $E_t = 0.21$ eV, the Langevin cross section admits complexes with $J < 312$. The centrifugal barrier at $MCTS_{C_2H_6}$ cuts off $k_{C_2H_6}$ near $J = 305$, which sets the limit on the range of J that contribute to the $Ni(C_2H_4)^+ + C_2H_6$ products. The centrifugal barrier at the exit channel TS'_{orb} does not further limit J, even under the extreme assumption that all angular momentum brought to the complex becomes orbital angular momentum in products ($l = l'$). The centrifugal barrier at $MCTS_{H_2}$ cuts off k_{H_2} near $J = 300$. The dotted portion of the curve ($J \geq 77$) represents the collision complexes that can surmount the centrifugal barrier at $MCTS_{H_2}$ but would be cut off by the angular momentum constraints in the exit channel TS''_{orb} under the strong assumption $l = l''$. In the CH_4 elimination channel, the upper limits on J set by $MCTS_{CH_4}$ and TS'''_{orb} are 261 and 250, respectively. The exothermicities used for these cutoff estimates for C_2H_6, CH_4, and H_2 channels are the experimental values of 23.1, 23.1, and 32.3 kcal/mol, respectively.[13]

In Figure 11 we show the model instantaneous decay rate into all four channels vs time at $E_t = 0.21$ eV. The overall decay of the complex is highly nonexponential. Decay of complexes to $Ni(C_2H_4)^+ + C_2H_6$ dominates on short time scales. The instantaneous ratio of rates for C_2H_6 formation to Ni^+ formation is drastically reversed from 50:1 at $t = 0$ μs to 1:26 at $t = 20$ μs. This is in sharp contrast with $Ni^+ + C_3H_8$,[7] where return of complexes to Ni^+ dominates the branching on all time scales. The reason is that the model MCTSs lie much further below reactants for $Ni^+ + n\text{-}C_4H_{10}$ than for $Ni^+ + C_3H_8$. The ratio of C_2H_6 to H_2 production varies only slightly, from 2:1 at $t = 0$ μs to 3:1 at $t = 10$ μs, consistent with the observation of a mild increase in the ratio $NiC_2H_4^+/NiC_4H_8^+$ as t_{ext} increases from 1 to 10 μs. The model ratio of C_2H_6/CH_4 production varies more than a factor of 100, from 22:1 at $t = 0$ μs to 2400:1 at $t = 10$ μs, whereas experiment finds slightly more CH_4 elimination in the longer time window. Experiment shows that a majority of the elimination products are formed on 100 ns−20 μs time scale

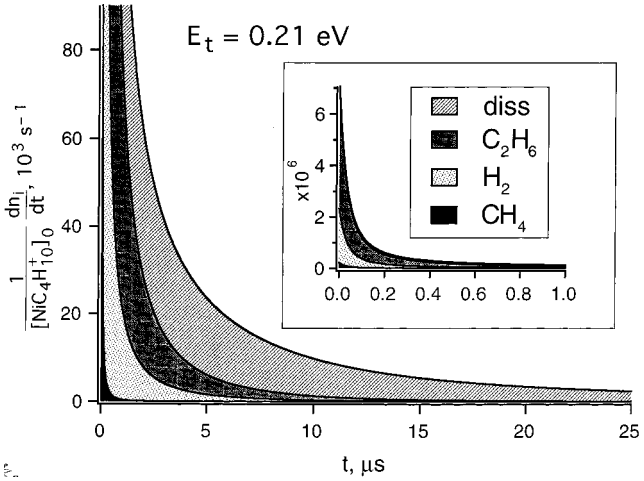

Figure 11. Instantaneous decay rate into competing fragmentation channels for adjusted model of $Ni^+ + n\text{-}C_4H_{10}$ (Table 6) at $E_t = 0.21$ eV.

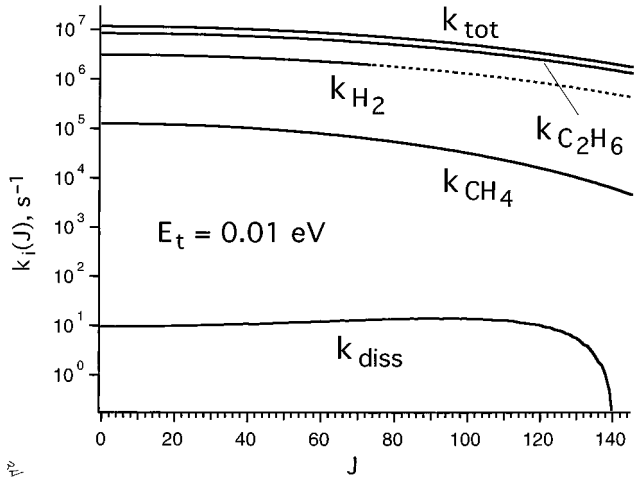

Figure 12. Microscopic parallel decay rates $k_i(E,J)$ for adjusted model of $Ni^+ + n\text{-}C_4H_{10}$ (Table 6) at $E_t = 0.01$ eV as a function of J. Dashed line is H_2 products that would be cut off by exit channel centrifugal effects under the strong assumption $l = l''$, as described in text.

for $E_t = 0.21$ eV. In qualitative agreement, the model predicts that only about 0.2% of the total elimination products are formed at $t \geq 20$ μs.

Our experiment in effect integrates such rate curves over various time intervals.[7] In Tables 1 and 2 we compare the adjusted model results with experimental data over the two ranges of time studied with $t_{ext} = 8$ μs. At $E_t = 0.21$ eV, the agreement between model and experiment is sensible over both the short ($t = 2-10$ μs) and medium ($t = 16-24$ μs) time windows. The model was explicitly adjusted to match these branching fractions well. In addition, the effects of kinetic energy and deuterium substitution are also well matched by the model calculations, which suggests the model is quite realistic.

2. Additional Kinetic Energy and Isotope Effects. In Figure 12 we show plots of the four model parallel decay rates and $k_{tot}(E,J)$ for the lower collision energy studied in the experiment, nominal $E_t = 0.01$ eV. These calculations include no internal energy in reactants. The Langevin cross section now admits complexes with J up to 145. As a consequence of this smaller range of J, the total decay rates now lie in a relatively narrow band from about 10^6-10^7 s^{-1}. These model rates are fast enough to explain the observation of substantial complex decay on the time scale of our experiment, 100 ns$-$20 μs. The return to reactants (k_{diss}) has shut down almost completely. Now k_{tot} is dominated by $k_{C_2H_6}$ for all J. Integration of the detailed decay rates vs t predicts that the fraction of total products seen as C_2H_6 in the mass spectrum taken at $t_{ext} = 8$ μs should increase from 51% at $E_t = 0.21$ eV to 74% at nominal $E_t = 0.01$ eV, in rough agreement with experiment (Table 1). The model predicts the experiment should see no intact complexes in the early time window. The experimental fraction of intact complexes decreases significantly, from 19% at $E_t = 0.21$ eV to 11% at nominal $E_t = 0.01$ eV. This qualitative agreement is encouraging, since prior to the modeling an increase in long-lived complexes as energy increased seemed counter-intuitive. The effect is due to the very different range of Js admitted by the Langevin cross section at the two different collision energies.

We also investigated the model effects of deuterium isotopic substitution for $Ni^+ + n\text{-}C_4D_{10}$. For the deuterated case, we calculate a complete set of vibrational frequencies and moments of inertia for the key stationary points and proceed as before, using the MCTS energies as adjusted to best fit the branching data and time scale observed for $Ni^+ + n\text{-}C_4H_{10}$ at 0.21 eV. Table 3 shows the energetic effects of deuteration. Deuteration has only a very small effect on the relative energy of the complex **1** or TS_{CC} and the CC insertion intermediate, as might be expected. The relative energy of $MCTS_{H_2}$ increases by about 2 kcal/mol. The energy of $MCTS_{CH_4}$ increases by 3.6 kcal/mol. In Tables 1 and 2 we compare the model results with experimental data. At 0.21 eV, deuteration increases the fraction of adducts from 19% to 53% for $t_{ext} = 8$ μs in the experiment. The model predicts 52%. The main cause is an increase in the density of states of the complex on deuteration. For $n\text{-}C_4H_{10}$, experiment finds that in the $2-10$ μs time window, C_2H_6 elimination is favored over H_2 elimination by about a factor of 2. For $n\text{-}C_4D_{10}$, the experimental ratio of C_2D_6 to D_2 elimination increases to 4. In the modeling, C_2D_6/D_2 increases from 2 for $n\text{-}C_4H_{10}$ to 20 for $n\text{-}C_4D_{10}$. These model results reflect a larger first-order isotope effect on the relative energy of $MCTS_{H_2}$ compared to $MCTS_{C_2H_6}$ upon deuteration.

For both $n\text{-}C_4H_{10}$ and $n\text{-}C_4D_{10}$, the experiments found fast dissociation of the complexes on the time scale of several hundred nanoseconds. We infer this from the metastable decay tails on the $NiC_2H_4^+$ and $NiC_2D_4^+$ peaks for short t_{ext}, as shown in Figure 1 and described in Section III. For $n\text{-}C_4H_{10}$, the best-fit single-exponential lifetime was 400 ns for both $E_t = 0.01$ eV and $E_t = 0.21$ eV. On deuteration to $n\text{-}C_4D_{10}$, the fitted lifetime lengthens to 750 ns (Figure 3), but the overall fit is less successful.

Comparison of Figures 10 and 12 makes it qualitatively clear how the shortest fragmentation time scale can be quite insensitive to collision energy. The adjusted model finds nonexponential decay at both collision energies, but the effects of J are stronger at 0.21 eV. The fastest rates occur at low J, where the centrifugal effects are smallest and $k_{C_2H_6}$ dominates at both energies. The model finds that the fastest k_{tot} increases only from 10^7 s^{-1} at $E_t = 0.01$ eV to 3×10^7 s^{-1} at $E_t = 0.21$ eV. The important point is that the total energy is varying only from 0 to 0.2 eV while the relevant MCTSs lie some 0.5 eV below the reactant asymptote, so the fastest decay rate changes slowly with E_t.

Since the model decay is nonexponential, we have approximately parametrized its predictions by the ratio of the integrated intensity of the narrow component of the TOF-MS peak (arising from fragmentation prior to the ion extraction pulse) to the integrated intensity of the broader tail (arising from fragmentation during ion acceleration, insets of Figures 1 and 3). In the model, this intensity ratio can be obtained by

integrating the decay rate curve for C_2H_6 elimination (Figure 11) over appropriate time intervals. For $n\text{-}C_4H_{10}$ at 0.01 eV, the model ratio is 1.83. At 0.21 eV collision energy, the model ratio is 1.82, remarkably insensitive to collision energy. For C_4D_{10}, the model ratio decreases to 0.68. For a single-exponential decay, specifying this intensity ratio would be equivalent to specifying a lifetime. Thus the model at least qualitatively explains why we can reasonably fit the experimental tails for $NiC_4H_{10}^+$ at both 0.01 and 0.21 eV to the same exponential lifetime and also why the $NiC_4D_{10}^+$ tail at 0.21 eV fits to a longer lifetime.

In further qualitative agreement with experiment, the model finds the ratio of C_2H_6 to H_2 elimination to be essentially independent of extraction time for $t_{ext} = 1-8$ μs. This corroborates the simplified kinetics model using a single long-lived complex as the precursor to all fragmentation paths.

VI. Discussion

Our approach has been to assume that the B3LYP calculations are sufficiently accurate to determine the lowest energy pathways to the majority elimination products, C_2H_6 and H_2. By discarding all calculated higher energy pathways, we limit the mechanism to two dominant ones. Both C_2H_6 and H_2 arise from the same initial central CC insertion step. The branching occurs subsequently when one β-hydrogen migrates to form $Ni^+(C_2H_6)(C_2H_4)$ over $MCTS_{C_2H_6}$ or two β-hydrogens migrate to form $Ni^+(H_2)(C_2H_4)_2$ over $MCTS_{H_2}$.

B3LYP theory thus provides a novel view of the $Ni^+ + n$-butane reaction mechanism. For many years, it had been postulated that C_2H_6 elimination arose from formation of a $Ni^+(H)(C_2H_5)(C_2H_4)$ intermediate from either of two pathways: initial central CC insertion followed by β-hydrogen migration or initial primary CH insertion followed by β-ethyl migration. From the $Ni^+(H)(C_2H_5)(C_2H_4)$ intermediate, C_2H_6 elimination competed with subsequent β-hydrogen migration to form $Ni^+(H_2)(C_2H_4)_2$, from which H_2 elimination occurred.[35,36] Like the old mechanism, the new one is completely consistent with previous experimental data on deuterium isotope effects,[29,31] which show very strong preferences for $C_2H_2D_2$, D_2, and CHD_3 elimination from $CD_3CH_2CH_2CD_3$. It is also consistent with the inference from collision-induced dissociation[30,32] that the structure of the $NiC_4H_8^+$ product is in fact $Ni^+(C_2H_4)_2$.

It is not possible to prove a mechanism. However, we have shown that the new, simplified mechanism based on electronic structure calculations and statistical rate theory applied to a single potential energy surface is in semiquantitative agreement with experiment when the key MCTS energies are adjusted downward. Many puzzling aspects of the data such as the nonexponential decay of complexes despite controlled energy, the larger fraction of adducts observed at higher collision energy, and the insensitivity of the fastest elimination time scales to collision energy can be understood readily from the effects of angular momentum conservation on the fragmentation time scale and branching.

We have now applied the same approach to two reactions, $Ni^+ + n\text{-}C_4H_{10}$ and $Ni^+ + C_3H_8$.[7] In both cases, the agreement between a simplified mechanism grounded in electronic structure calculations and the experimental cross sections, branching fractions, complex decay time scales, and deuterium isotope effects is quite satisfying. Perhaps the weakest aspects of the RRKM modeling involve the treatment of the soft degrees of freedom. It is again encouraging that a consistent treatment across both reactions is comparably successful. The two mechanisms themselves are satisfyingly consistent in the sense that the lowest energy pathways involve breaking of the weakest bond or bonds of the alkane. In $Ni^+ + C_3H_8$, the predominant CH_4 elimination channel arises from CC insertion and passage over the appropriate MCTS. The minority H_2 elimination channel arises from insertion into the secondary CH bond. In $n\text{-}C_4H_{10}$, as we have seen, both C_2H_6 and H_2 can arise from insertion into the central CC bond, the weakest bond in the molecule. The next lowest energy pathway to H_2 breaks a secondary CH bond again. In all cases, it is only necessary to invoke β-hydrogen migrations at the MCTSs. Theory consistently finds that β-alkyl migrations lead to MCTSs at much higher energy.

If the mechanism is correct at least at low collision energies, the quantitative accuracy of the MCTS energies from B3LYP still needs significant improvement for theory to become a more useful predictive tool. In the present study of $Ni^+ + n\text{-}C_4H_{10}$, we had to adjust $MCTS_{C_2H_6}$ downward by 2−3 kcal/mol from the calculated value and $MCTS_{H_2}$ downward by 7 kcal/mol. For the $Ni^+ + C_3H_8$ reaction, we adjusted $MCTS_{CH_4}$ downward by 5−6 kcal/mol and $MCTS_{H_2}(2°)$ downward by 7 kcal/mol. Clearly B3LYP is systematically overestimating the MCTS energies. It would be very useful to test what level of electronic structure theory is needed to bring these barrier heights into better agreement with experiment.

The nature of the MCTSs themselves (Figure 9) pays tribute to the resourcefulness of gas-phase transition-metal cations in their disassembly of alkanes. With nine valence electrons and only six low-lying valence orbitals (the five 3d orbitals and the 4s orbital), Ni^+ simply cannot carry out the stepwise insertion, β-migration, elimination mechanism that was postulated for many years. The 4p orbitals do not participate in gas-phase bonding, as evidenced by many electronic structure calculations and by the experimental fact that the lowest $3d^74p$ state of Ni^+ lies at 6.4 eV. The optimal bonding interaction[37] of Ni^+ with alkene involves two metal orbitals (two donor−acceptor interactions): doubly occupied metal dπ donating into empty alkene π^* and empty metal sdσ accepting from doubly occupied alkene π. The Ni^+ configuration for insertion into the central CC bond of *n*-butane is presumably $3d^84s^1$(low-spin doublet), as in the a^2F atomic state at 1.7 eV. However, using two sd hybrids to form the two σ bonds in $Ni^+(C_2H_5)_2$ leaves only a single half-occupied orbital as possible σ-acceptor from an alkene donor plus three doubly occupied 3d orbitals for π-donation into alkene antibonding orbitals. There is simply not sufficient bonding capacity to form a stable intermediate such as $Ni^+(C_2H_5)(H)(C_2H_4)$, much less $Ni^+(H)_2(C_2H_4)_2$, as the old stepwise pathways required. The solution to this dilemma seems to be the MCTSs, which in effect bypass the need for stepwise intermediates. Based on earlier calculations,[7,27,28,38] Fe^+ and Co^+ evidently share this dilemma with Ni^+.

Examination of the structures in Figure 9 shows that the Ni^+ center is simultaneously interacting with as many as four hydrogen atoms and incipient alkene groups combined. In particular, note the rather short Ni^+- -H distances between metal and migrating hydrogen in both $MCTS_{H_2}$ and $MCTS_{C_2H_6}$. The +1 charge on Ni contributes to the stability of the MCTSs. The charge also leads to significant agostic interactions between the positive metal center and the CH bonds of certain methyl groups.[28] These attractive interactions, closely akin to hydrogen bonding, may stabilize certain MCTSs by 5 kcal/mol or more, which is quite significant. The geometric signature of such an agostic interaction is a lengthening of CH bonds within the methyl group. The strongest effects seem to occur for β- and γ-methyl groups. At this level of theory, a normal methyl group

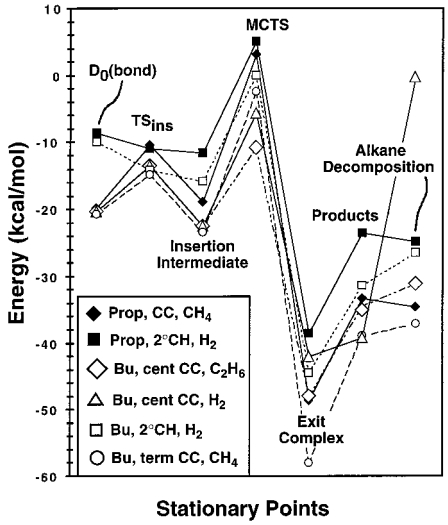

Figure 13. Comparison of stationary point energies from B3LYP theory for various reaction paths in $Ni^+ + C_3H_8$ ("Prop" in legend) and $Ni^+ + n\text{-}C_4H_{10}$ ("Bu" in legend). "D_0(bond)" and "Alkane Decomposition" are experimental data for alkane bond dissociation energies and for decomposition to the reaction products of interest for each channel. These two categories have been adjusted by arbitrarily adding −107 kcal/mol for D_0(bond) and −53 kcal/mol for alkane decomposition to bring them onto the same scale as the B3LYP energies for the Ni^+ reactions. See text for detailed explanation.

has CH bond lengths within a range of about 0.01 Å (roughly 1.088−1.102 Å), depending on orientation and the nature of the vicinal bonds. In $Ni^+ + n\text{-}C_4H_{10}$, we note the 1.164 Å CH bond in the β-methyl group of $MCTS_{C_2H_6}$ (Figure 9). Also noteworthy but not shown are a 1.122 Å CH bond in the γ-methyl group of both the terminal TS_{CC} and the terminal CC insertion intermediate **5**. The last examples for *n*-butane are a 1.122 Å CH bond in the γ-methyl group of the secondary CH insertion TS and a 1.131 Å CH bond in the β-methyl group of $MCTS_{H_2}(2°)$. In $Ni^+ + C_3H_8$, we found a corresponding 1.134 Å CH bond within the β-methyl group of $MCTS_{H_2}(2°)$. Theoretical work on the strength of such agostic interactions would be very useful for qualitative thinking.

If we are to understand the subtleties of product branching in these reactions, we must begin to understand the relative energetics of the key multi-center transition states with resolution of several kcal/mol or better. It is informative to compare the B3LYP energies of key stationary points for the various pathways in both $Ni^+ + C_3H_8$ and $Ni^+ + n\text{-}C_4H_{10}$ on the same scale with known experimental bond dissociation energies and decomposition energies of the starting alkanes. We do so in Figure 13 for six reaction pathways. For $Ni^+ + C_3H_8$, the data include the two lowest energy paths, CC insertion leading to CH_4 elimination and secondary CH insertion leading to H_2 elimination.[7] For $Ni^+ + n\text{-}C_4H_{10}$, the data include central CC insertion leading to both C_2H_6 and H_2 elimination, terminal CC insertion leading to CH_4 elimination, and secondary CH insertion leading to H_2 elimination.

The column of data plotted at the far left labeled "D_0(bond)" is the bond dissociation energy at 0 K[39] of the bond into which Ni^+ inserts, either CC or CH bonds of various types. At the far right, labeled "Alkane Decomposition", is the 0 K gas-phase enthalpy change ΔH_0[39] for decomposition of the starting alkane into the same products formed by Ni^+ (one or two of which are alkenes that remain bound to Ni^+). For example, for central CC insertion in $n\text{-}C_4H_{10}$ and eventual formation of $NiC_2H_4^+ + C_2H_6$, it is ΔH_0 for the process $n\text{-}C_4H_{10} \rightarrow C_2H_4 + C_2H_6$. In two cases, that of $D_0(2\text{-}C_4H_9\text{-}H)$ and of the decomposition energy of $n\text{-}C_4H_{10} \rightarrow$ 2-butene + H_2, the data are values at 298 K. These probably differ from the 0 K values by only 1−2 kcal/mol, which will not affect any of our conclusions.

The rest of the plotted data are unadjusted B3LYP calculated energies of the various stationary points relative to reactants and corrected for zero-point energy. TS_{ins} is the transition state between the Ni^+(alkane) complex and the bond insertion intermediate, in turn labeled Insertion Intermediate. MCTS is the multi-center transition state en route to the appropriate Exit Complex, and Products are the elimination products. The two columns of experimental data were adjusted by an arbitrary additive constant in order to place D_0(bond) and the alkane decomposition energy on roughly the same level as insertion intermediate and products, respectively. The constant was −107 kcal/mol for D_0(bond) and −53 kcal/mol for alkane decomposition.

A variety of comparisons are then informative. First, D_0(bond), the alkane decomposition energy, and the product energy all track each other fairly well. To a first approximation, the bond dissociation energy determines the thermochemistry of the alkane decomposition process of interest. The reaction products differ from the alkane decomposition energy only by the energy of association of an alkene with Ni^+, which is fairly independent of the identity of the alkene. The glaring exception is the alkane decomposition for the channel $2C_2H_4 + H_2$, which makes and breaks different numbers of bonds from the five other examples and thus lies on a different scale entirely.

Starting from the left side of the diagram, we can see at a glance that the 10−12 kcal/mol difference in bond energies between CH and CC bonds is not mirrored in the insertion transition state energies TS_{ins}, which vary only 5 kcal/mol. At TS_{ins}, the larger CH bond energy is evidently compensated by a smaller "intrinsic barrier" for CH vs CC insertion, perhaps due to steric constraints or the adverse effects of greater orbital directionality in the CC case. This is not nearly so large an effect as suggested earlier.[35] This difference has little impact on product formation, since all TS_{ins} energies lie far below reactants. The insertion intermediate wells recover much of the breadth of the bond dissociation energies.

Specific comparisons of pathways within one reaction and between the two reactions are helpful. For example, CC insertion in propane becomes central CC insertion in *n*-butane on "mutation" of a terminal hydrogen into methyl. The energetics of the corresponding stationary points (filled and open diamonds in Figure 13) track each other quite closely for D_0(bond), Exit Complex, and Products, but the *n*-butane energies lie 3−4 kcal/mol lower at TS_{ins} and the Insertion Intermediate and a remarkable 14 kcal/mol lower at the MCTS. We interpret this to mean that $MCTS_{C_2H_6}$ in the *n*-butane reaction is anomalously stable by some 5−10 kcal/mol. At least part of the reason is likely the attractive agostic interaction between the metal center and the β-methyl group which arises in the "mutation". The geometric evidence for this interaction was detailed above. This is the longest CH bond we have found. There is no corresponding strong agostic interaction at the insertion intermediate $C_2H_5{-}Ni^+{-}C_2H_5$, and indeed it is only slightly more stable than the propane analogue.

Similarly, we can compare CC insertion in propane with terminal CC insertion in *n*-butane (filled diamonds and open circles). Despite very similar bond energies and alkane decomposition energies, the *n*-butane path now lies 4 kcal/mol lower at TS_{ins} and the insertion intermediate, 9 kcal/mol at the exit complex, and 5.6 kcal/mol at the key MCTS. As described above, we find strong geometric evidence of a γ-methyl agostic

interaction in both TS_{ins} and $CH_3-Ni^+-CH_2CH_2CH_3$. The exit complex is also more stable for *n*-butane due to the stronger binding of propene vs ethylene, a recurring theme in Figure 13. Evidently the extra stability of the insertion intermediate and exit channel complex carry over into the MCTS lying between these two wells, as might be expected.

Comparing the secondary CH insertion paths toward H_2 elimination for propane and *n*-butane (filled and open squares), we find that all five stationary points track each other closely, with *n*-butane increasingly stable by 3−6 kcal/mol going from left to right in the diagram. Again, it seems that the extra stability of the insertion intermediate, exit complex, and products confers extra stability on the MCTS as well.

Finally, the novel double β-hydrogen migration pathway to H_2 elimination (open triangles) via $MCTS_{H_2}$ closely tracks the two secondary CH insertion pathways toward H_2 (filled and open squares) at the insertion intermediate and the MCTS, but not at the exit channel. The special stability of $MCTS_{H_2}$ seems to be related to its unique ability to produce H_2 products from initial insertion into the weak central CC bond, rather than a much stronger CH bond. This advantage seems to carry over to the unusual MCTS. The exit channel complex for the same path lies at nearly the same energy as the products because the two available empty or half-filled valence orbitals on Ni^+ are already involved in bonding to the two alkenes.

How widespread is the phenomenon of multi-center transition states? Electronic structure calculations have found such MCTSs to be important in reactions of Fe^+,[27,38] Co^+,[28] and Ni^+ [7] with small alkanes. This may be due to the large number of doubly occupied 3d orbitals on the right-hand side of the 3d series and the large exchange energy associated with pairing additional electrons. Recently, Armentrout and co-workers[26] have suggested that Ru^+ (seven valence electrons, isoelectronic to Fe^+) in fact reacts with alkanes via the stepwise mechanism. The rationale[39] is that the promotion energy to a lower spin state of configuration d^6s^1 (^2G) is only 1.35 eV in Ru^+, compared with 1.96 eV in Fe^+.[40] Such a configuration allows two σ bonds plus a full donor−acceptor interaction with alkene. On the left-hand side, where empty d orbitals are available for donor−acceptor interactions with alkenes, the stepwise mechanism may again dominate. There is room for much more theoretical work in this area.

VII. Conclusion

The combination of B3LYP calculations with statistical rate theory on a single potential energy surface can explain essentially all of the experimental observations for the Ni^+ + *n*-butane reaction at low collision energy. In both Ni^+ + *n*-butane and Ni^+ + *n*-propane, the same types of multi-center transition states play a critical role in determining reaction efficiency and product branching. The presence or absence of agostic interactions between metal and β- and γ-methyl groups significantly influences the relative energies of different pathways. Despite our adjustment of the key $MCTS_{C_2H_6}$ and $MCTS_{H_2}$ downward to lie 13−14 kcal/mol below reactants, centrifugal barriers still have a substantial effect on the time scale of the reaction for the largest *J* sampled within the Langevin cross section. In future work, we will extend this approach to the reactions of Co^+ with propane, *n*-butane, and isobutane in order to test whether B3LYP captures the substantial effects of the change in metal identity on product branching.

Acknowledgment. J.C.W. thanks the National Science Foundation (CHE-9616724) and the donors of the Petroleum Research Foundation (PRF-33441-AC6) for generous support of this research. R.J.N. gratefully acknowledges support from a Department of Education fellowship and a Procter and Gamble Fellowship. S.S.Y. acknowledges support from a Lubrizol Fellowship.

References and Notes

(1) Becke, A. D. *J. Chem. Phys.* **1993**, *98*, 1372.
(2) Eller, K.; Schwarz, H. *Chem. Rev.* **1991**, *91*, 1121.
(3) Armentrout, P. B.; Baer, T. *J. Phys. Chem.* **1996**, *100*, 12866.
(4) Weisshaar, J. C. In *Gas-Phase Metal Reactions*; Fontijn, A., Ed.; Elsevier: Amsterdam, 1992.
(5) Blomberg, M. R. A.; Siegbahn, P. E. M.; Svensson, M. *J. Chem. Phys.* **1996**, *104*, 9546.
(6) Noll, R. J.; Yi, S. S.; Weisshaar, J. C. *J. Phys. Chem.* **1998**, *102*, 386.
(7) Yi, S. S.; Blomberg, M. R. A.; Siegbahn, P. E. M.; Weisshaar, J. C. *J. Phys. Chem.* **1998**, *102*, 395.
(8) Noll, R. J.; Weisshaar, J. C. *J. Am. Chem. Soc.* **1994**, *116*, 10288.
(9) Noll, R. J. Ph.D. Dissertation, University of Wisconsin-Madison, 1994.
(10) Hunt, W. W.; Huffman, R. E.; Saari, J.; Wassel, G.; Betts, J. F.; Paufve, E. H.; Wyess, W.; Fluegge, R. A. *Rev. Sci. Instrum.* **1964**, *35*, 88.
(11) Baer, T.; Hase, W. L. *Unimolecular Reaction Dynamics*; Oxford University Press: New York, 1996.
(12) Robinson, P. J.; Holbrook, K. A. *Unimolecular Reactions*; Wiley-Interscience: New York, 1972.
(13) Gilbert, R. G.; Smith, S. C. *Theory of Unimolecular and Recombination Reactions*; Blackwell Scientific Publications: Oxford, U.K., 1990.
(14) Sanders, L.; Hanton, S. D.; Weisshaar, J. C. *J. Chem. Phys.* **1990**, *92*, 1990.
(15) Hanton, S. D.; Noll, R. J.; Weisshaar, J. C. *J. Chem. Phys.* **1992**, *96*, 5176.
(16) Fuhr, J. R.; Martin, G. A.; Wiese, W. L. *J. Phys. Chem. Ref. Data* **1988**, *17*, Suppl. 4.
(17) Page, R. H.; Gudeman, C. S. *J. Opt. Soc. Am.* **1990**, *B7*, 1761.
(18) Wiley: W. C.; McLaren, I. H. *Rev. Sci. Instrum.* **1955**, *26*, 1150.
(19) Gallagher, R. J. Ph.D. Thesis, Yale University, 1972.
(20) Lee, C.; Yang, W.; Parr, R. G. *Phys. Rev. B* **1988**, *37*, 785.
(21) Frisch, M. J.; Trucks, G. W.; Schlegel, H. B.; Gill, P. M. W.; Johnson, B. G.; Robb, M. A.; Cheeseman, J. R.; Keith, T. A.; Petersson, G. A.; Montgomery, J. A.; Raghavachari, K.; Al-Laham, M. A.; Zakrzewski, V. G.; Ortiz, J. V.; Foresman, J. B.; Cioslowski, J.; Stefanov, B. B.; Nanayakkara, A.; Challacombe, M.; Peng, C. Y.; Ayala, P. Y.; Chen, W.; Wong, M. W.; Andres, J. L.; Replogle, E. S.; Gomperts, R.; Martin, R. L.; Fox, D. J.; Binkley, J. S.; Defrees, D. J.; Baker, J.; Stewart, J. P.; Head-Gordon, M.; Gonzalez, C.; Pople, J. A. *Gaussian-94*, Revision A.1; Gaussian, Inc.: Pittsburgh, PA, 1995.
(22) Hay, P. J.; Wadt, W. R. *J. Chem. Phys.* **1985**, *82*, 299.
(23) Wachters, A. J. H. *J. Chem. Phys.* **1970**, *52*, 1033.
(24) Ricca, A.; Bauschlicher, C. W. *Chem. Phys. Lett.* **1995**, *245*, 150.
(25) Sievers, M. R.; Jarvis, L. M.; Armentrout, P. B. *J. Am. Chem. Soc.* **1998**, *120*, 1891−1899.
(26) Armentrout, P. B.; Chen, Y.-M. *J. Am. Soc. Mass Spectrom.* **1999**, in press.
(27) Holthausen, M. C.; Koch, W. *Helv. Chim. Acta* **1996**, *79*, 1939.
(28) Holthausen, M. C.; Koch, W. *J. Am. Chem. Soc.* **1996**, *118*, 9932.
(29) Halle, L. F.; Houriet, R.; Kappes, M. M.; Staley, R. H.; Beauchamp, J. L. *J. Am. Chem. Soc.* **1982**, *104*, 6293.
(30) Jacobson, D. B.; Freiser, B. S. *J. Am. Chem. Soc.* **1983**, *105*, 5197.
(31) Hanratty, M. A.; Beauchamp, J. L.; Illies, A. J.; van Koppen, P. A. M.; Bowers, M. T. *J. Am. Chem. Soc.* **1988**, *110*, 1.
(32) Jacobson, D. B.; Freiser, B. S. *J. Am. Chem. Soc.* **1983**, *105*, 736.
(33) Langevin, P. *Ann. Chim. Phys.* **1905**, *5*, 245.
(34) Pollak, E.; Pechukas, P. *J. Am. Chem. Soc.* **1978**, *100*, 2984.
(35) van Koppen, P. A. M.; Brodbelt-Lustig, J.; Bowers, M. T.; Dearden, D. V.; Beauchamp, J. L.; Fisher, E. R.; Armentrout, P. B. *J. Am. Chem. Soc.* **1991**, *113*, 2359.
(36) Houriet, R.; Halle, L. F.; Beauchamp, J. L. *Organometallics* **1983**, *2*, 1818.
(37) Blomberg, M. R. A.; Siegbahn, P. E. M.; Svensson, M. *J. Phys. Chem.* **1992**, *96*, 9794.
(38) Holthausen, M. C.; Fiedler, A.; Schwarz, H.; Koch, W. *J. Phys. Chem.* **1996**, *100*, 6236.
(39) Perry, J. K. Ph.D. Thesis, California Institute of Technology, 1994.
(40) Sugar, J.; Corliss, C. *J. Phys. Chem. Ref. Data* **1985**, *14*, Suppl. 2.